# A Low-Cost Fluorometer Applied to the Gulf of Saint Lawrence Rhodamine Tracer Experiment

Kyle T. Park, *Member, IEEE*, Joshua J. Creelman, Allison S. Chua, Teala S. Chambers, Aaron M. MacNeill, *Member, IEEE*, and Vincent J. Sieben

Abstract—In order to increase the spatiotemporal resolution and accessibility of freshwater and marine data, low-cost in situ fluorometers are required. The devices must be robust, fully submersible, and sensitive in the 1 ppb–1 ppm range for compounds such as Rhodamine water tracer (RWT), a dye used in time of travel, and substance dispersal measurements. In this work, we introduce a deployment-ready, low-cost, small form-factor RWT fluorometer prototype based on the principle of lock-in amplification. Using measurements collected from remotely operated underwater vehicle (ROV) deployments during a dye-tracer experiment in the Gulf of Saint Lawrence, we compare its performance against that of a widely used commercial fluorometer. The results of the prototype's calibration and deployment show competitive performance against commercial instruments, with a limit of detection (LOD) below 0.2 ppb and for a cost of U.S. $744.70, a fraction of the cost of relevant commercially available in situ fluorometers.

Index Terms— Chlorophyll, fluorometer, harmful algal bloom (HAB), lock-in amplifier, low cost, Rhodamine, sensor.
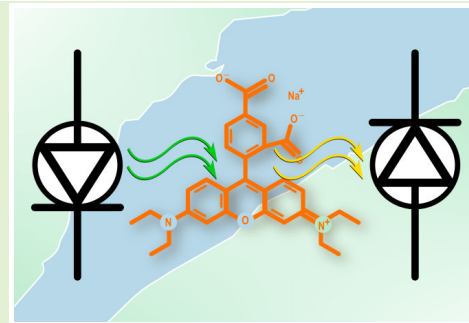
I. INTRODUCTION

THE growing focus on the health of our rivers and oceans demands wider reaching, higher resolution, and more broadly accessible data. Science vessels collecting water samples for laboratory analysis have given way to rapid in situ analysis using remotely operated underwater vehicles (ROVs), underwater gliders, and autonomous laboratories such as the ARGO floats. These platforms, while flexible, require sensors that perform like their benchtop counterparts while being compact, submersible, and low enough cost to deploy at the scale of the data needed.

The submersible in situ fluorometer is a powerful tool for the direct measurement and surveillance of fluorescent compounds (fluorophores) for a variety of applications [1]. Ultraviolet fluorescence can be used to detect and assess crude oil spills [2]. The fluorescence of chlorophyll-a [3] and phycoerythrin [4], [5] is used to monitor [6] the development of harmful algal blooms (HABs). Fluorescent dissolved organic matter (fDOM) is an indicator of overall biological activity [1]. Dye-tracer studies map the movements of rivers and ocean currents by releasing inert fluorescent dyes such as Rhodamine water tracer (RWT) into the water and tracking its concentration across time, space, and depth with a fluorometer [7], [8].

Patents assigned to companies still active in the submersible fluorometer space date at least as far back as 1979 [9] assigned to Chelsea Instruments Ltd., now Chelsea Technologies (Molesey, West Molesey, U.K.). Similarly, Turner Designs (San Jose, CA, USA) states that they have provided over 75 000 fluorometers since 1972 in their datasheets. By 1997, Chelsea's tethered "AQUATracka MK III" submersible fluorometer was in active research use detecting chlorophyll-a in situ [10], [11]. In 1998, the "DIVING-PAM" (WALZ, Germany), a submersible in vivo chlorophyll fluorometer to be carried by SCUBA divers, was introduced [12]. This self-contained device required no tether but was bulky and expensive by modern submersible fluorometer standards.

TABLE I
CHARACTERISTICS OF SELECT COMMERCIAL FLUOROMETERS

Manufacturer	Fluorometer	Target	Length (cm)	Diameter (cm)	LOD (ppb)	Price[a] (USD)
WALZ	DIVING-PAM	Chlorophyll	39	19	-	22000
Chelsea	AQUATracka III	Chlorophyll-a	40.5	8.8	0.01	-
	UviLux	fDOM	14.9	7	0.02	-
	TriLux	Chlorophyll-a	14	2.6	0.1	-
Turner	Cyclops-7F	Chlorophyll-a	14.5	2.2	0.03	-
	Cyclops-7F	RhodamineWT	14.5	2.2	0.01	-
Sea-Bird	ECO-FL	Chlorophyll-a	12.7	6.3	0.02	5800
	ECO-FL	RhodamineWT	12.7	6.3	0.05	7800
Seapoint	Chlorophyll	Chlorophyll-a	16.8	6.4	0.02	3800
	Rhodamine	RhodamineWT	16.8	6.4	0.02	3800

[a]Listed prices are from Q4 2022 / Q1 2023 for all entries except DIVING-PAM (2016 price), as quoted to an academic institution (Dalhousie University).

Most contemporary submersible fluorometers follow the Chelsea/Turner model and are configured to target a single fluorophore. Some are configured with multiple channels to target multiple fluorophores independently. These systems can also perform nonfluorometric measurements such as turbidity.

Chelsea Technologies markets their "UviLux" fluorometers for water quality assessment and oil detection, as well as a three-channel "TriLux" fluorometer for HAB detection and monitoring algae. The TriLux has a limit of detection (LOD) of 0.1 ppb chlorophyll-a. In this context, 1 ppb is defined as a concentration of 1 μg/L.

Turner Designs markets their popular [6], [13] "Cyclops-7F" line of submersible fluorometers, with LODs of 0.01 ppb for RWT and 0.03 ppb for chlorophyll-a.

Sea-Bird Scientific (Bellevue, WA, USA) produces the "ECO-FL" line of submersible single-channel fluorometers, having LODs of 0.02 ppb for chlorophyll-a and 0.05 ppb for RWT.

Seapoint Sensors (Exeter, NH, USA) also produces a self-titled line of fluorometers, with an LOD of 0.02 ppb for both chlorophyll-a and RWT.

The characteristics of these fluorometers, along with their most recent available price, are summarized in Table I. A conservative estimate of the market size of these fluorometers is in the tens of thousands.

The common LOD across the described devices is 0.02 ppb with the Turner device being as low as 0.01 ppb for Rhodamine, though this does not necessarily extend to other fluorophores. The cost range of submersible fluorometers is U.S. $3400–U.S. $7000 (2022 $) per channel depending on the target fluorophore [14], [15], [16] and U.S. $>20 000 for benchtop fluorometers [3], [14], [15], and as of 2013, there were no commercially relevant submersible fluorometers available for less than U.S. $1325 (1000 €, 2013) [16].

There is also competing work to produce fluorometers below the U.S. $1000 threshold. Zieger et al. [17] developed a four-channel fluorometer prototype for algal classification for under U.S. $400. However, the design is a flowthrough type known to be less convenient and effective in underwater field use [3]. Flowthrough systems have added complexity
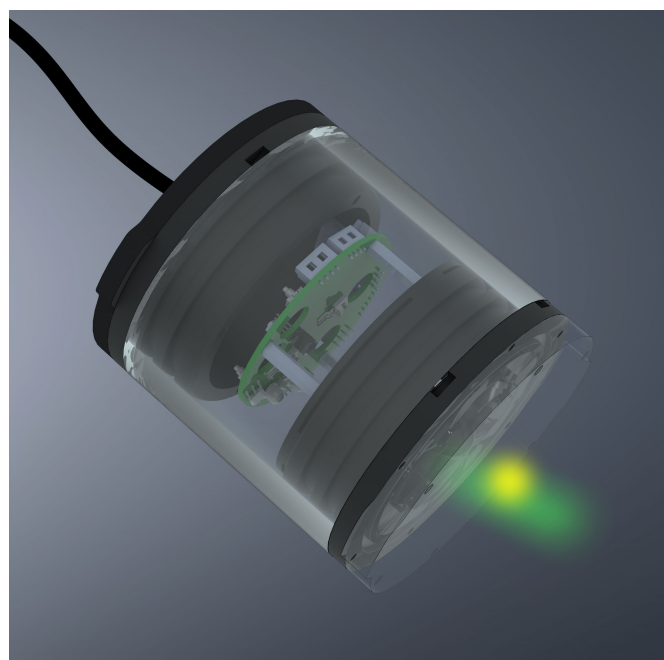

Fig. 1. Prototype fluorometer in CAD, illustrating submersible in situ RWT fluorometry. Water directly in front of the device is illuminated with green light, and Rhodamine's yellow fluorescence is collected in return. A tether supplies power and returns data to the surface.

with fluid pumping and in dealing with biofouling on enclosed optical windows. Haidekker et al. [18] designed a one-channel in vivo chlorophyll fluorometer for U.S. $300 [18]. The device illuminates samples in free space (i.e., benchtop only) and is not yet ported into a submersible housing, which would add significant cost. While there are reports of low-cost fluorometers, there remains a need to realize submersible and low-cost fluorometers that compare well with commercial instrument performance.

In this work, we present a novel in situ fluorometer ready to use at depth for U.S. $744.70 based on off-the-shelf components, 3-D-printed parts, and an advanced signal processing scheme; the digital lock-in amplifier. The prototype fluorometer uses a sinusoidal modulation of LED light to produce excitation and emission that pulsates at the same

TABLE II
PROTOTYPE FLUOROMETER BOMs

Component	Product Name	Manufacturer or Supplier	Location	Price (USD)
Clear Acrylic End-cap	Clear Acrylic End Cap (3" Series)	BlueRobotics	Torrance, CA, USA	9.2
Cast Acrylic Tube	Cast Acrylic Tube (3" Series)	BlueRobotics		13.79
O-Ring Flange x2	O-Ring Flange (3" Series)	BlueRobotics		44.14
Custom Acrylic end cap	9M001	Acrylite	Sanford, USA	2.85
SubConn connector	Micro Circular 6M connector	MacArtney	Nova Scotia, Canada	138.8
LED	LED525-33	Roithner Lasertechnik GmbH	Vienna, Austria	3.23
LED Collimating lens	5.0 mm Dia. x 7.5 mm FL, Uncoated, Plano-Convex Lens, stock number #48-652	Edmund Optics Inc.	New Jersey, USA	30.78
Photodiode Collimating lens	25 mm Dia x 20 mm FL, Uncoated Molded Aspheric Condenser Lens, stock number #36-168	Edmund Optics Inc.		24.47
Focusing lens	10.0 mm Diameter, N-BK7 Half-Ball Lens, stock number #45-937	Edmund Optics Inc.		42.58
Excitation filter	550 nm 12.5 mm Diameter, OD 4.0 Shortpass Filter, stopband 562 nm to 825 nm, stock number #84-695	Edmund Optics Inc.		135.43
Emission filter	578 nm CWL, 12.5 mm Dia, 16 nm Bandwidth, OD 6 Fluorescence Filter, stock number #87-738	Edmund Optics Inc.		176.47
Photodiode	TSL257	Digi-Key	Minnesota, USA	1.29
Custom PCB				116.3
Miscellaneous[a]				5.36
Total				**744.7**

[a]Miscellaneous components include PLA spools for 3D-printing, screws, washers, and jumper wire.

modulation frequency so that the fluorescence can be distinguished from sources of noise and interference. The prototype targets RWT fluorescence, but other fluorophores can be targeted by swapping optoelectronics and optical filters with drop-in replacements with no added complexity. A rendering of the prototype and an illustration of in situ RWT fluorometry are presented in Fig. 1.

We calibrated our prototype alongside two representative commercial RWT fluorometers and demonstrated comparable performance. Following calibration, we deployed our prototype along with a commercial fluorometer on an ROV in the Dalhousie University Aquatron Laboratory (Dalhousie University, Halifax, NS, Canada). This platform was then used in a field comparison study in the Gulf of Saint Lawrence of northeastern Canada for the purpose of time of travel and substance dispersal measurements. The work was performed under the Marine Environmental Observation Prediction and Response Network (MEOPAR, Halifax, NS, Canada) and Reseau Quebec Maritime (RQM, Rimouski, QC, Canada) Tracer Release Experiment (TReX), an RWT experiment conducted between September 5 and 9, 2021.

From the laboratory to the field, our novel prototype fluorometer offers comparable performance to commercial systems, at a fraction of the cost.

II. MATERIALS AND METHODS

A. Novel Fluorometer

The single-channel prototype fluorometer presented in this work is fully submersible to a depth of at least 500 m and has a mass of 400 g and a volume of less than 380 cm^3. It costs U.S.
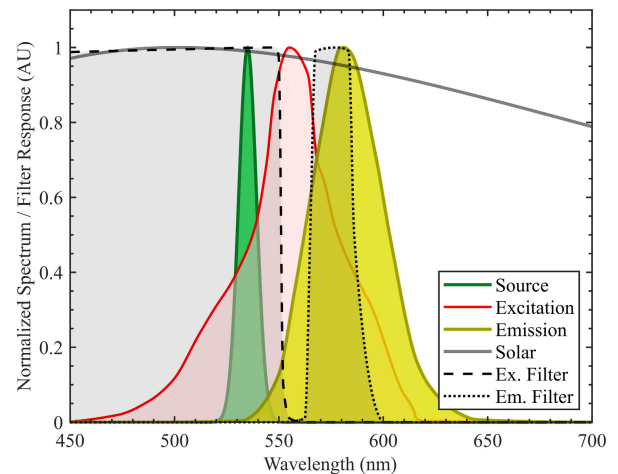

Fig. 2. Normalized spectra/filter responses of the chosen optical source, the excitation and emission of RWT, the solar background, and the chosen excitation and emission filters. Filter responses ensure the rejection of the overlapped source and emission spectra and the rejection of solar spectrum before the optical detector.

$744.70 to assemble at the time of authorship, substantially less than the purchase price of relevant commercial competitors [3], [14], [15], [16], using only two custom components. The prototype targets RWT, which is maximally excited by 555-nm light and exhibits peak emission at 580 nm [7].

The prototype is housed in prefabricated, off-the-shelf cylindrical components by BlueRobotics (Torrance, CA, USA). The interior structural components are 3-D-printed in polylactic acid (PLA) using the CreatorPro 3-D-printer by FlashForge
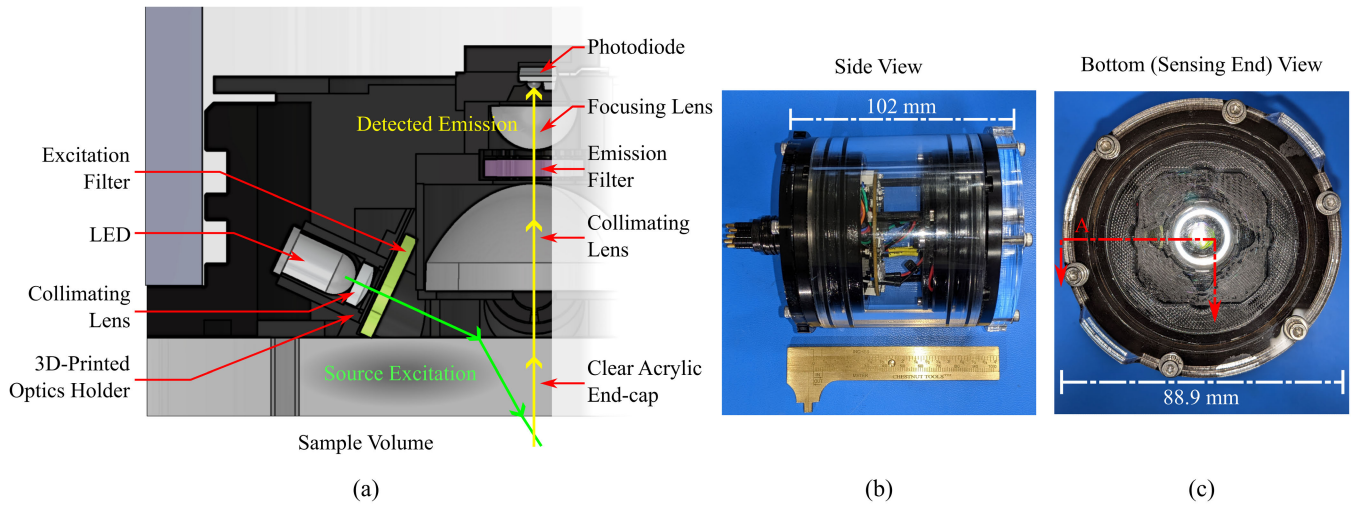
Fig. 3.   (a) Sectioned view of the optical system with all key features labeled. (b) Side view of the realized prototype with 4.5 in caliper for scale. (c) Bottom (sensing end) view of the realized prototype. The red section lines denoted "A" indicate the section view used in (a).

(Jinhua, Zhejiang, China) with default tolerance settings. Black PLA filament is used to absorb stray light inside the fluorometer. The optics are sourced from Edmund Optics (Barrington, NJ, USA) and are mounted and aligned in the fluorometer using 3-D-printed housings.

A black-tinted custom acrylic endcap is hand-milled from 6-mm acrylic stock to match the profile and screw-hole locations of the BlueRobotics clear acrylic endcap.

A custom PCB, repurposed from another project, controls the device. It is interfaced using RS-232 through a six-pin SubConn connector. An architecture diagram of the custom PCB is included in the Appendix. A purpose-driven PCB redesign would be significantly cheaper. The prototype's bill of materials (BOM) is presented in Table II.

B. Optical Design

Our optical design task was to create an optical stack that exposes a sample volume of seawater with excitation in direct view of the optical detector. The stack must use only off-the-shelf or 3-D-printed components.

The optical source must overlap the excitation spectrum of RWT, while optical filters must reject the overlap between the source and emission spectra to minimize optical interference (i.e., crosstalk from reflection and backscattering) and must reject background noise (i.e., solar spectrum intrusion). Fig. 2 shows the wavelength spectra and filter responses of the chosen optical stack components, the excitation and emission spectra of RWT from Laidlaw and Smart [7], and the worst case solar spectrum (i.e., neglecting atmospheric and aquatic absorbances). The spectrum of the optical detector used in this work is relatively flat over this wavelength range and is excluded for clarity.

As required in our design task, Fig. 2 shows that the narrowband emission filter passes RWT fluorescence while rejecting most of the solar spectrum and rejects the band of wavelengths where the source and excitation spectra overlap. The excitation filter further minimizes the overlap between the source and the emission spectra in the case where temperature increases or part variations shift the source spectrum to the right.
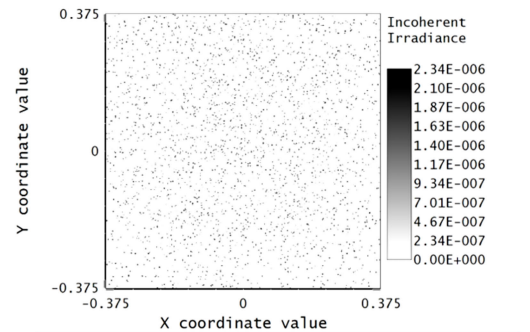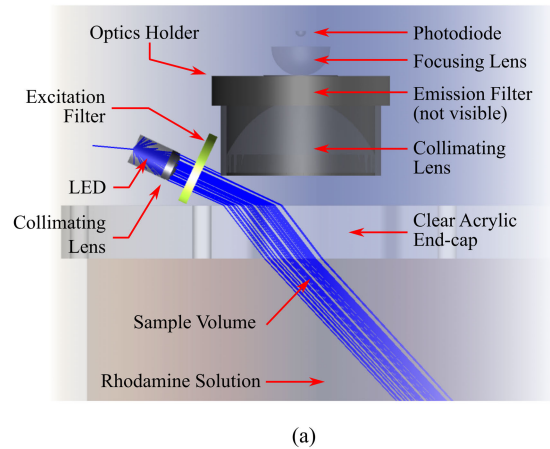

Fig. 4.   (a) Side view of the 3-D model of the optical stack used in OpticStudio simulations. The blue lines are rays used for simulating LED emissions. (b) Optic Studio simulation output as a 2-D scatter plot of fluorescence rays striking the photodiode. The detected optical power indicated in red is used for simulated calibration.

In our design, a green LED optical source is aligned with a collimating lens, and the excitation filter matched to the excitation spectrum peak of RWT. The filtered and collimated

excitation transmits through the clear acrylic endcap where it illuminates a sample volume of seawater.

If present, the Rhodamine will fluoresce in response and this emission is collected by a collimating lens. The collected light is filtered by the emission filter matched to the emission spectrum peak of RWT so that only RWT fluorescence passes. The collimated emission is then focused onto a detecting photodiode, with integrated transimpedance amplifier, by a hemispherical focusing lens. The specifications and names of these parts can be found in the BOM, see Table II.

Fig. 3(a) presents a sectioned view of the optical system in our prototype. The optics, optical source and detector, sample volume, and optical paths of the excitation and emission are labeled for clarity. Fig. 3(b) shows the prototype photographed in a side view. Fig. 3(c) shows the prototype photographed in a bottom (or sensing end) view, with superimposed sectioning lines used to indicate the view presented in Fig. 3(a).

C. Ray-Tracing Simulations

Prior to realizing the prototype fluorometer, we simulated the optical stack with Zemax OpticStudio to optimize its design [19]. The model and the simulation output are shown in Fig. 4.

OpticStudio performed 3-D ray tracing to test the lens-filter stack, simulate the photodiode's response to fluorescence, and optimize feature placement. The ray-tracing model includes the prototype's opaque housing to block stray rays, and a fluorescing volume characterized to match the refractive index and flourescence spectra of RWT dissolved in seawater with a typical [20] quantum yield of 31%. The LED is simulated as a point source of rays, whereas the photodiode is simulated as a subsystem of three parts: a clear lens, a thin aperture, and a square detecting area. The volume of water interrograted by the sensor—the sample volume—is approximately 1.2 cm^3.

Fig. 4(a) offers a side view of the bundle of rays, colored blue, produced by the LED. Fig. 4(b) shows the simulated irradiance pattern detected by the photodiode. The coordinates of each dot represent where a fluorescence ray strikes the simulated photodiode and the grayscale of each dot represents that ray's irradiance. The output of the simulation is taken as the total incident optical power detected by the photodiode, indicated in the red box. The simulations are repeated for a range of RWT concentrations in the sample volume, each requiring approximately three days to complete.

The total incident optical power results from the OpticStudio simulations are entered into a simple spreadsheet that simulates the photodetector's photocurrent and transimpedance amplifier responses. The spreadsheet produces a simulated calibration curve, plotting amplifier output voltage per sample Rhodamine concentration (molarity). The simulated calibration curve is shown in Fig. 5, illustrating the expected linear ($R^2 > 0.99$) relationship between fluorophore concentration and detector voltage.

D. Laboratory-Based Calibration and Verification

The prototype, along with two representative instruments of currently available technology to compare to the prototype's
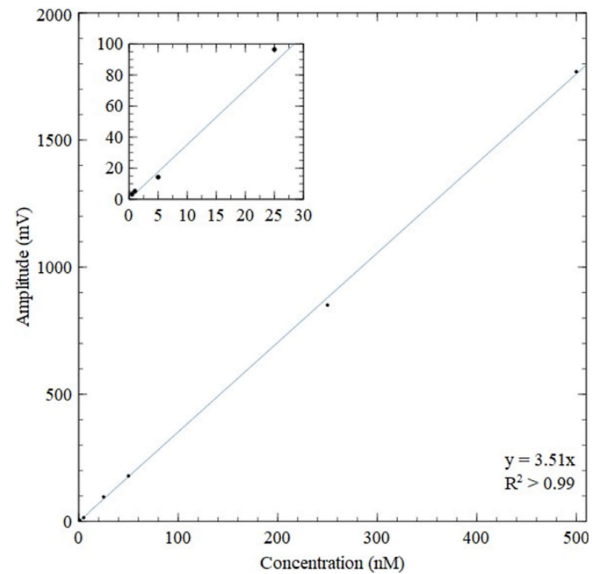

Fig. 5. Zemax OpticStuido simulated photodetector voltage response Rhodamine concentration versus user-set Rhodamine concentration for ray-tracing experiments.

performance, was taken to the CERC.OCEAN Laboratory at Dalhousie University and calibrated against known standards of RWT prepared in solution with seawater from the Aquatron Laboratory. The Aquatron houses seawater tanks ranging from small purpose-driven containers to six larger tanks totaling over 2000 m^3 of seawater pumped from the Northwest Arm (Halifax, NS, Canada), making it an extremely attractive location to reliably simulate in situ testing.

Rhodamine WT 400 ppb (Turner Designs, San Jose, CA, USA) standards were each prepared in 2-L beakers by dilution with seawater dispensed from the Aquatron to target concentrations of 0.5, 2, 10, 30, and 60 ppb, as well as a blanking standard of undyed seawater, 0 ppb. These concentrations are chosen from past deployments indicating that the observable range of RWT was between 0.5 and 60 ppb [19].

The RWT standards were measured using three fluorometers: the prototype, a Turner Cyclops-7 (Turner Designs, San Jose, CA, USA), and an AML X2Change powered by Turner Designs (AML oceanographic, Dartmouth, NS, Canada). The prototype and AML devices stream digital data, whereas the Turner device is analog and is measured with a multimeter (Model number 34460A, Keysight Technologies, Kanata, ON, Canada). The commercial devices have three manual gain settings (1×, 10×, 100×) and are set to 10×, whereas the prototype needs no adjustment across its sensitive range.

For each calibration point, the standard in its 2-L beaker was placed in a temperature bath housed inside a light-blocking chamber and kept well-mixed using a magnetic stirrer. The tested sensor was mounted with the sensing end submerged in the solution and pointed down, axially aligned with the beaker at a consistent height across all three devices. A Lauda Eco Gold immersion thermostat (Lauda, Delran, NJ, USA) was suspended in the bath. Each standard is cycled through 5 °C, 8 °C, 11 °C, 14 °C, 17 °C, and 20 °C equilibria, taking approximately 1 h to reach each desired temperature. At each equilibrium, each sensor sequentially collected 5 min worth of
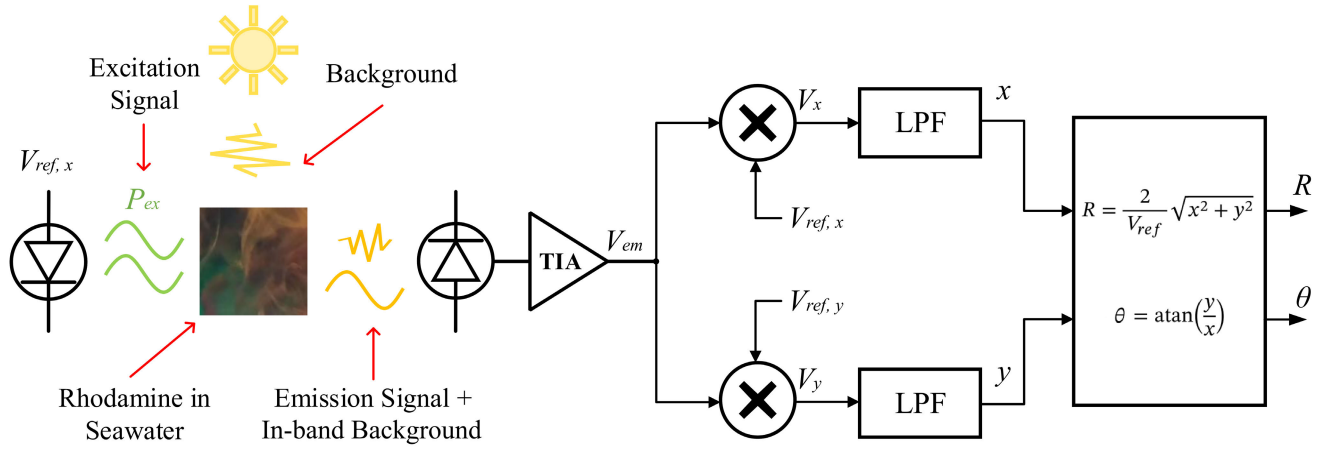
Fig. 6. Simplified lock-in RWT fluorometer block diagram. The LED generates an excitation signal from a known sinusoidal reference $V_{\text{ref},x}$. Excitation enters the sample volume and RWT fluoresces if present. This emission carries the same modulation frequency as the excitation at a longer optical wavelength. The emission, with superimposed in-band background noise and interference, is detected by the photodiode. The detected photocurrent is converted to voltage and mixed with in-phase and in-quadrature references, $V_{\text{ref},x}$ and $V_{\text{ref},y}$ respectively. The resulting signals are low-pass filtered and then used to compute R and θ.

data. When the sensors were switched, extra time was taken to allow the bath to return to the desired temperature equilibrium before data collection resumed.

E. Large Tank Study and Field Deployment

After calibration, the larger tanks in the Aquatron Laboratory were used to deploy the fluorometers in a controlled environment [19]. The prototype and the AML fluorometer were mounted to a BlueROV2 (BlueRobotics). The ROV was driven through plumes of RWT as it was dispensed, recording the agreement in the RWT concentration reported by the two fluorometers.

Finally, the prototype was deployed along with the Turner Cyclops-7 (standard version of their "Fast" 7F variant) during MEOPAR's TReX, mounting them to the same ROV used in the Aquatron testing. The TReX deployments occurred on September 5–9, 2021. Each day 300 L of 1% RWT was dispensed over a period of approximately 4 min into the Gulf of Saint Lawrence, just north of Rimouski, QC, 48°35′01.0″N, 68°31′08.8″W just before noon, except on the 9th where 900 L of 0.44% RWT was dispensed over a period of approximately 6 min. Rhodamine concentration time series were recorded, along with ROV depth, to show how the prototype performs in a head-to-head comparison with an industrial representative, with favorable results.

F. Lock-In Fluorometry

One aspect of this prototype fluorometer is that it uses digital lock-in amplification to extract sinusoidally modulated emission signals from the targeted fluorophore. An all-digital lock-in design has advantages in cost and complexity over the expensive and bulky analog-mixer alternative, as the algorithm is implemented on the same microprocessor that handles device control and data interfacing.

A fluorometer that implements a lock-in amplifier (a lock-in fluorometer) has performance advantages compared to the conventional constant-level illumination approach. Fig. 6 presents a simplified block diagram for a lock-in fluorometer.

The signal of interest (i.e., emitted fluorescence) is captured and processed at an intermediate frequency. This separates the signal from low-frequency noise such as amplifier red noise or the in-band component of sunlight that is not rejected by the optical emission filter, preventing signal corruption that is unavoidable in a constant-illumination approach.

The sample volume is illuminated with a modulated excitation signal that is produced by the LED and is in-phase with and identical in frequency to the lock-in reference, $V_{\text{ref},x}$. A percentage (the quantum yield) of the photons absorbed by the fluorophore in solution results in emission of new photons at a longer wavelength. When an excited fluorophore molecule returns directly to the ground state and emits a photon, this emission is fluorescence [21] and the process occurs over a natural lifetime typically on the nanosecond timescale or 1–5 ns for the Rhodamine family of dyes [22].

Since the natural lifetime τ is much shorter than the modulation period of the excitation signal (0.1–10 ms in our case or 0.1–10 kHz), the emission signal detected at the photodiode is proportional to and time-shifted relative to the excitation signal produced by the LED, whereas only the ac signal components are relevant, if the excitation signal $P_{\text{ex}}(t)$ is described by the following:

$$P_{\text{ex}}(t) = P \cos(2\pi f_l t) \tag{1}$$

where P is the peak excitation optical power produced by the LED and f_l is the frequency of the lock-in amplifier reference; then, the ideal emission signal detected at the photodiode and converted to voltage by its supporting electronics $V_{\text{em}}(t)$ is described by the following:

$$V_{\text{em}}(t) = R \cos(2\pi f_l t - \theta) \tag{2}$$

where R is proportional to the concentration of the dissolved fluorophore in the sample volume and

$$\theta \approx 2\pi f_l \tau \tag{3}$$

is the phase shift in the emission signal, relative to the lock-in reference, caused by the natural lifetime of the fluorescence
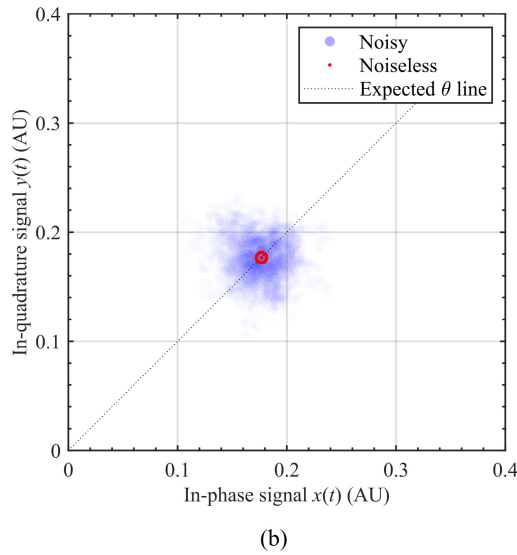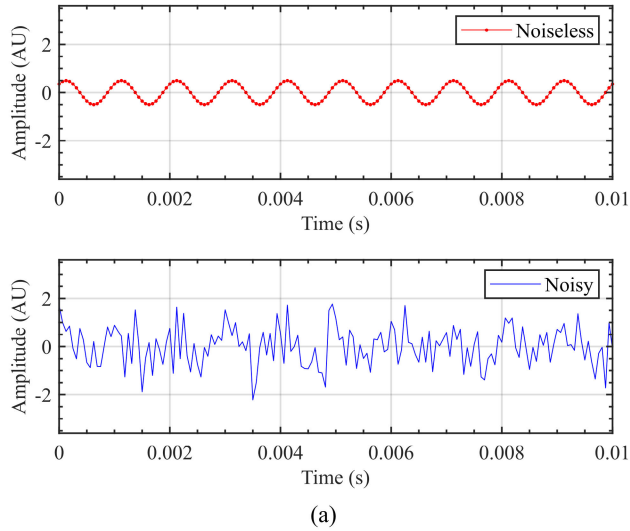
(a)

(b)

Fig. 7. (a) Plots of simulated emission signals, presented in noiseless (top in red) case and noisy with white noise superimposed on the noiseless case. (b) Coordinate plot of in-phase and in-quadrature lock-in signals. Distance from origin represents $R/2$ and angle from horizontal represents θ. Noiseless red circled dot indicates perfect recovery of R and θ, whereas blue cloud approximates central tendency and joint distribution of the remaining noise on $x(t)$ and $y(t)$.
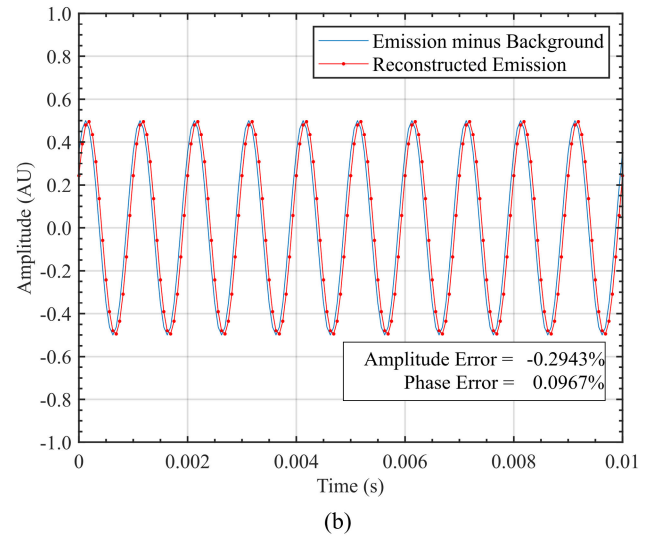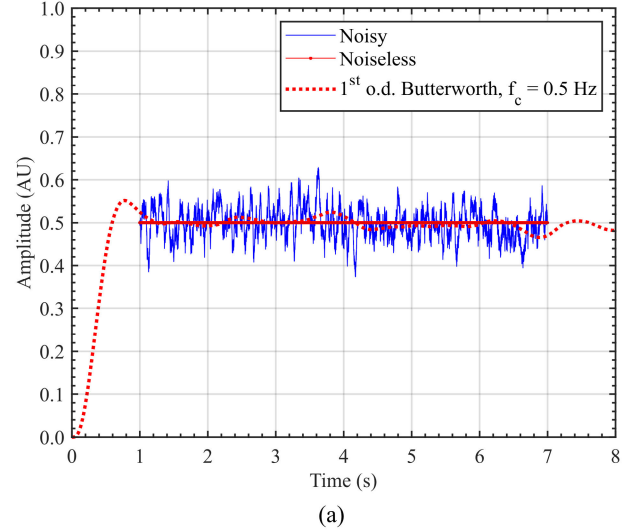

(a)

(b)

Fig. 8. Output of lock-in amplifier. (a) Time series of R computed by a lock-in amplifier. Noisy and noiseless results presented along with the first-order Butterworth low-pass filtered noisy case showing transients. (b) Comparison plot of simulated emission signal (before noise is superimposed) and the emission signal as reconstructed using mean values of R and θ. The reconstructed signal differs by less than 1% in each of R and θ.

process. The emission signal is mixed with voltage signals in-phase and in-quadrature with the lock-in reference, creating a pair of intermediate signals each containing a sum-frequency component and a difference-frequency (in this case, dc) component. The intermediate signals are then fed through low-pass filters to remove the sum-frequency component, producing an in-phase signal $x(t)$ and an in-quadrature signal $y(t)$. If the amplitude of the references used in the mixers is V_{ref}, then these signals can be described by the following:

$$x(t) = \frac{1}{2} V_{ref} R \cos\theta \tag{4}$$

and

$$y(t) = \frac{1}{2} V_{ref} R \sin\theta. \tag{5}$$

From (4) and (5), equations for R and θ directly follow:

$$R = \frac{2}{V_{ref}} \sqrt{x^2(t) + y^2(t)} \tag{6}$$

$$\theta = \mathrm{atan}\left(\frac{y(t)}{x(t)}\right). \tag{7}$$

While this basic treatment considers R and θ to be constants, the analysis and its results are directly applicable to slowly varying cases of either (or both). In practice, background noise and interference, such as solar-spectrum intrusion, reflections and scattering, or incidental fluorescence, is injected into the system in the detection process making R and θ estimates of their ground-truth values.

To illustrate the benefit of the lock-in fluorometer over the conventional dc approach, a lock-in amplifier is simulated in

MATLAB. A reference signal is generated at 1 kHz and used to produce a background-and-noise-free emission signal with an amplitude of 0.5 arbitrary units (AU) and a phase shift of 45° relative to the reference signal. In this case, the ideal values of R and θ are 0.5° and 45°, respectively. A pure white Gaussian noise signal is generated with signal power that, in the mean squared sense, is four times that of the emission signal for a signal-to-noise ratio of 0.25 or −6 dB. This is also the signal-to-noise ratio in the comparable dc approach.

The simulated emission signal, both noiseless and with noise, is shown in Fig. 7(a). After mixing and filtering with a simple sliding average filter (chosen for its simplicity and deliberately because of its poor filtering performance), the in-phase and in-quadrature signals $x(t)$ and $y(t)$ are plotted together on a coordinate plane, see Fig. 7(b). The red circled dot illustrates the ideal values of $x(t)$ and $y(t)$ extracted from the noiseless case and falling exactly on the expected 45° dashed line, whereas the blue dots are scattered due to the presence of noise.

Fig. 8 shows the output of the lock-in amplifier. In Fig. 8(a), the real-time computed value of R is presented in the noisy case, the noiseless (ideal) case, and the noisy case once again after filtering with a simple first-order Butterworth low-pass filter. In Fig. 8(b), the original background-and-noise-free emission signal is plotted next to a reconstruction of the emission signal using the average values of R and θ extracted from the noisy emission signal case. The final signal-to-noise ratios on R and θ are 22.7 and 19.7 dB, respectively. This is an improvement of 28.7 dB on R over the comparable dc approach, and an extraction of the phase change θ that a dc approach is completely insensitive to.

III. RESULTS AND DISCUSSION

A. Concentration and Temperature Calibration

The results of the laboratory-based calibration and verification are given in Fig. 9. In Fig. 9(a), the prototype sensor output is plotted against standard concentration, and curves are plotted for each of the equilibrium temperatures indicating strong linear relation ($R^2 > 0.99$) between sensor amplitude and RWT concentration as well as between slope (mV/ppb) and temperature. The linear fit of the temperature-dependent calibration curves is described by the following:

$$V_S - V_{\text{offset}} = S(T) C_S \qquad (8)$$

where C_S is the known RWT standard concentration, $S(T)$ is the slope of the calibration curve at known equilibrium temperature T, V_S is the voltage reading directly from the sensor at the known standard concentration and temperature, and V_{offset} is the offset (vertical intercept) of the linear fit.

The slope $S(T)$ of each fit is extracted and plotted against temperature in Fig. 9(b). This plot is also fit to a linear equation that yields the temperature-corrected relationship between sensor output and concentration (inset equation, top right) as described by the following:

$$S(T) = S_0 + S_1 T \qquad (9)$$

where S_0 and S_1 are the parameters of the linear fit. Fig. 9(c) shows the offset (intercept) of each fit plotted in Fig. 9(a).

Fig. 9(d)–(f) shows the equivalent set of calibration curves corresponding to the AML fluorometer, whereas Fig. 9(g)–(i) corresponds to the Turner fluorometer.

As the parameters of each fit are themselves random variables, the offsets provided in Fig. 9(c), (f), and (i) are subject to variance due to temperature-dependent noise and component parameters (i.e., temperature-dependent spectrum shifts), as well as component nonlinearities, quantization noise, and device alignment deviations in the calibration chamber between calibration trials. To compensate for this variance across temperatures, the mean offset $\tilde{V}_{\text{offset}}$ is computed.

The coefficients of these sequential linear fits, along with the mean offsets, are then used to form temperature-corrected equations for each fluorometer, and the generic equation for each is described by the following:

$$C = \frac{V_{\text{raw}} - \tilde{V}_{\text{offset}}}{S_0 + S_1 T} \qquad (10)$$

where C is the temperature-corrected measurement of RWT concentration in ppb and V_{raw} is the voltage reading directly from the sensor at the sample concentration and temperature. Equation (10) is used to process the subsequent precision, LOD, and deployment data.

The temperature dependence of fluorescence is known [7] to follow the exponential relationship described by the following:

$$F_S = F e^{n(T_s - T)} \qquad (11)$$

where F_S is the fluorescence of a standard at standard temperature T_S, F is the fluorescence of a sample at sample temperature T, and n is the temperature exponent.

Notably, the temperature dependence exhibited in Fig. 9 shows good agreement with the literature. For RWT, the temperature exponent is reportedly within the range of −0.027 °C^{-1} [23] to −0.026 °C^{-1} [7]. To a first approximation, the temperature exponent can be obtained from the linear fit parameters with the following equation:

$$n \approx S_1 / S_0. \qquad (12)$$

The approximate temperature exponents are −0.017 °C^{-1}, −0.016 °C^{-1}, and −0.017 °C^{-1} for the prototype, AML device, and Turner device, respectively. These results show remarkable concordance and are within 50% of reference values.

The results obtained for the prototype sensor are also in reasonably good agreement with their Zemax OpticStudio simulations. Qualitatively, both exhibit the expected linear response. Quantitatively, the half-amplitude output of the lock-in amplifier can be scaled by two to peak-to-peak amplitude to compare more directly to the dc-based OpticStudio output (a fair comparison when referred to the excitation LEDs output range). The simulated calibration curve achieves an output voltage of 300 mV at a concentration of 100 nM (approximately 56.7 ppb for RWT). The measured calibration curve achieves an output range between 200- and 320-mV
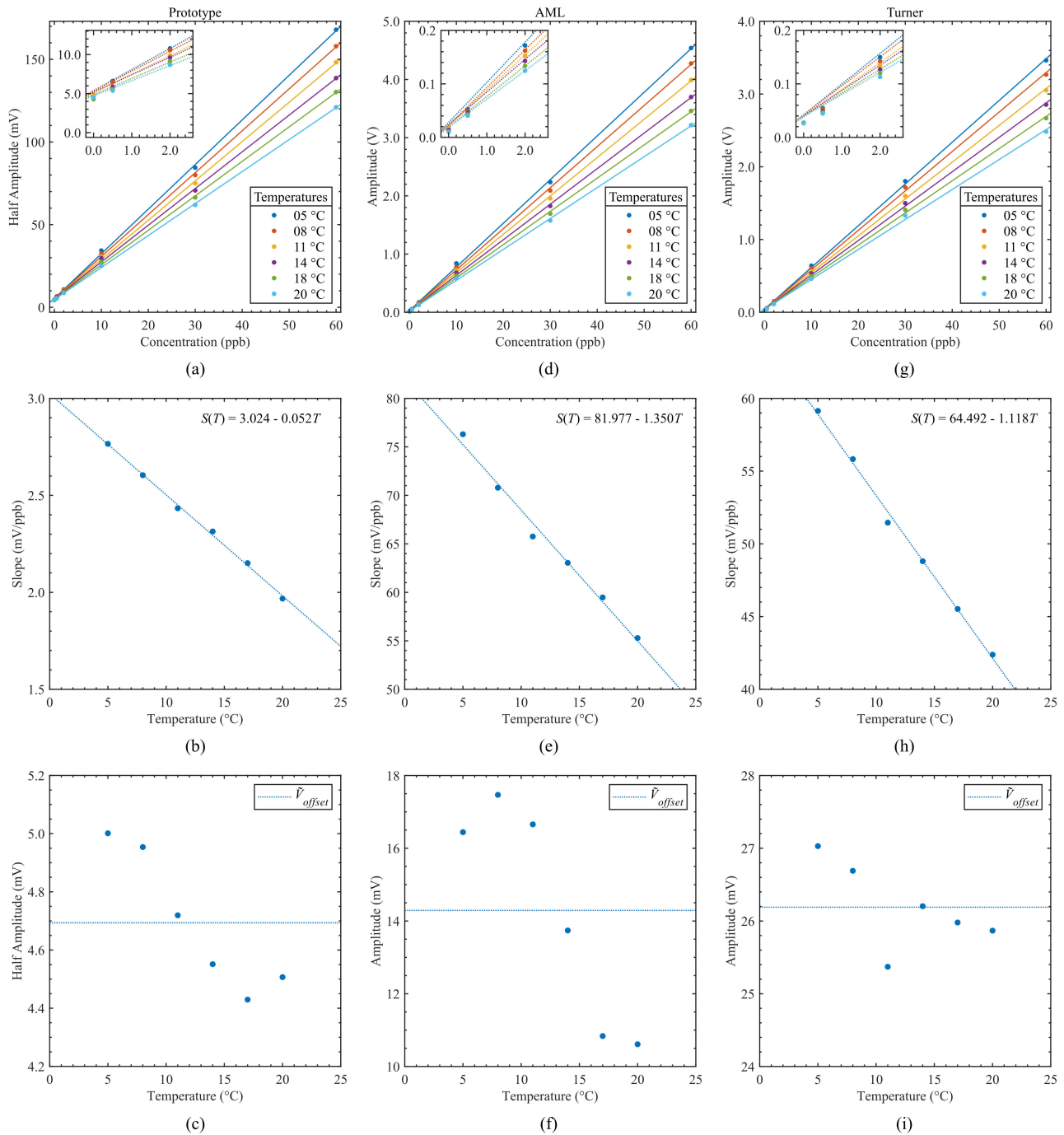
Fig. 9. Plots of output voltage against standard concentration with linear fit, slopes of the linear fits versus temperature, and offsets of the linear fits versus temperature. (a)–(c) Prototype fluorometer. (d)–(f) AML fluorometer. (g)–(i) Turner fluorometer.

peak-to-peak for the same concentration, depending on temperature. The simulated result is therefore accurate to within a factor of 2.

The quantitative discrepancy between the measured and simulated amplitudes, as well as between measured and referenced temperature exponents, can be attributed to unmodeled confounding factors such as the decaying quantum yield [7] over time in the presence of the sodium and potassium chlorides in seawater. Correcting the model for these minor factors is outside the scope of this work and is not strictly relevant to the calibration nor to the field testing

as they demonstrably affect each of the three fluorometers evenly.

B. Precision and Noise

Since the error bars are small relative to the full-scale calibration curves presented in Fig. 9, the standard deviations (SDs) of Fig. 9(a) can be found in Table III, similarly for Fig. 9(d) in Table IV and for Fig. 9(g) in Table V. The SDs are relatively stable and insensitive to both temperature and concentration, in all but a few anomalous points (indicated in red). This finding indicates an absence of heteroskedasticity

TABLE III
MEASUREMENT SD, PROTOTYPE CALIBRATION DATA

	Sample Temperature (°C)					
	5	8	11	14	17	20
Concentration (ppb)	Standard Deviation (mV)					
0	0.115	0.113	0.113	0.114	0.123	0.142
0.5	0.124	0.120	0.121	0.112	0.114	0.118
2	0.123	0.124	0.119	0.123	0.123	0.123
10	0.138	0.127	0.370	0.129	0.135	0.142
30	0.134	2.180	2.147	0.135	0.131	0.121
60	0.123	0.122	0.117	0.118	0.130	0.122

TABLE IV
MEASUREMENT SD, AML X2CHANGE CALIBRATION DATA

	Sample Temperature (°C)					
	5	8	11	14	17	20
Concentration (ppb)	Standard Deviation (mV)					
0	1.150	1.283	1.058	1.036	1.023	1.068
0.5	1.049	1.039	1.027	1.016	1.060	1.176
2	1.090	1.115	1.116	1.058	1.061	1.071
10	1.117	1.092	1.091	1.081	1.082	1.212
30	1.732	1.513	1.239	1.409	1.254	1.147
60	1.452	3.643	2.317	3.036	1.609	4.127

TABLE V
MEASUREMENT SD, TURNER CYCLOPS-7 CALIBRATION DATA

	Sample Temperature (°C)					
	5	8	11	14	17	20
Concentration (ppb)	Standard Deviation (mV)					
0	0.274	0.285	0.264	0.276	0.291	0.279
0.5	0.309	0.292	0.295	0.278	0.274	0.289
2	0.261	0.284	0.280	0.261	0.262	0.268
10	0.320	0.505	0.466	0.895	0.959	0.583
30	0.338	2.045	0.649	0.469	0.549	1.891
60	0.907	0.543	0.755	0.730	0.632	0.339

and therefore justifies the choice of line-of-best-fit linear regression.

The calibrations were performed in a light-blocking chamber, so the solar spectrum does not contribute variance to the measurement data. In integrated CMOS transimpedance devices such as TSL257, thermal noise is known [24] to be the dominant contributor of noise in the amplifier and therefore in the electronic subsystem. The Johnson–Nyquist thermal noise equation for resistance is given in the following equation:

$$|v_n| = 2\sqrt{k_B T R} \tag{13}$$

where k_B is Boltzmann's constant, T is the absolute temperature of the device in kelvin, and R is the resistance, which indicates that per root Hz of bandwidth and the SD due to thermal noise is proportional to the square root of the device's absolute temperature. However, as this proportionality is not meaningfully observed in any of Table III, Table IV, or Table V, other temperature-sensitive effects (i.e., spectral shifts in the optical source and detector) and temperature-insensitive sources of noise and interference (optical crosstalk and scattering of fluorescent emission) drown out the variance of thermal noise alone. To assess this, assuming that the variation in SD across concentrations is at least approximately normally distributed, Fig. 10 shows chi-squared confidence intervals (CIs) on the prototype variance data
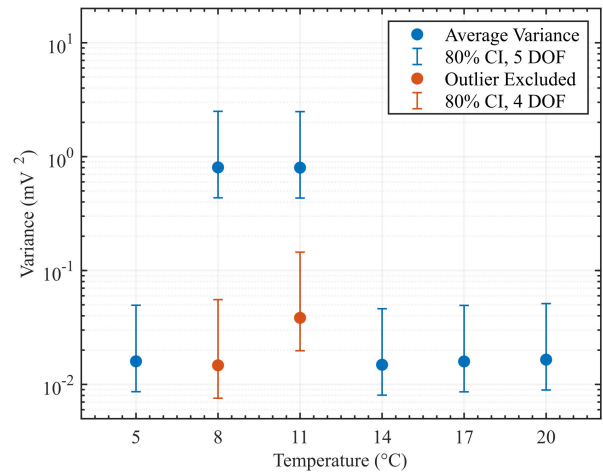

Fig. 10. Chi-squared 80% CIs for the prototype measurement variance across concentrations, per temperature. Due to the overlap between CIs, it cannot be said that the measurement variance monotonically increases significantly with temperature.

(SD squared). Even at the 80% confidence level used, all intervals overlap except those with anomalous entries, and those intervals overlap if the anomalous entries are excluded. Therefore, it cannot be said that the variance monotonically increases significantly with temperature. The same analyses are performed for the AML and Turner data and reach the same conclusion but are omitted for brevity.
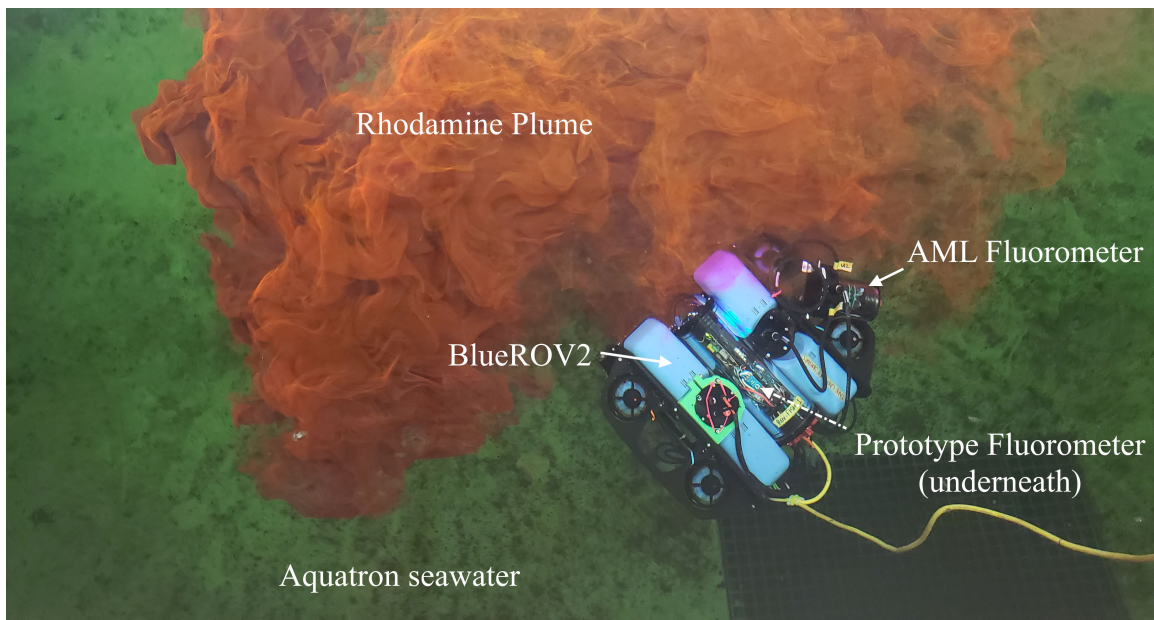
Fig. 11.   Photograph of the Dalhousie Aquatron Laboratory testing. The ROV equipped with the prototype and AML fluorometers can be seen approaching the first dose RWT plume.

TABLE VI
LOD PER SENSOR, PER TEMPERATURE

LOD(ppb)	5°C	8°C	11°C	14°C	18°C	20°C
Prototype	0.13	0.13	0.15	0.15	0.17	0.22
AML	0.046	0.054	0.047	0.049	0.052	0.058
Turner	0.014	0.015	0.015	0.017	0.019	0.02

TABLE VII
LOQ PER SENSOR, PER TEMPERATURE

LOQ(ppb)	5°C	8°C	11°C	14°C	18°C	20°C
Prototype	0.42	0.43	0.46	0.5	0.58	0.72
AML	0.15	0.18	0.16	0.16	0.17	0.19
Turner	0.047	0.051	0.051	0.057	0.064	0.066

The prototype calibration curve offsets have a mean, $\tilde{V}_{\text{offset}}$, of 4.69 mV and a standard error of 0.098 mV or 2% of the mean. This is superior to the AML device with $\tilde{V}_{\text{offset}}$ of 14.3 mV and a standard error of 1.24 mV or 8.7% of the mean and comparable to the Turner device with a $\tilde{V}_{\text{offset}}$ of 26.2 mV and a standard error of 0.24 mV or 1% of the mean. This indicates that the prototype has calibration repeatability that is within the range of commercially available fluorometers.

C. Limit of Detection

The LOD and limit of quantification (LOQ) are determined from the noise levels in each system using data collected in the blanking concentration (0 ppm) step of calibration. The literature [25], [26], [27], [28], and regulatory [29] standard "three-sigma" method is used, taking the LOD and LOQ to be three times and ten times the SD of the blanking test, respectively [30]. SDs are converted from volts to ppb by using (10) and setting $\tilde{V}_{\text{offset}}$ to zero.

Since higher temperatures yield weaker fluorescence for the same concentration, as described by (11), the LOD and LOQ are fundamentally increasing functions of temperature. In simpler terms, to obtain a voltage signal that is strong enough to exceed the LOD or LOQ threshold in voltage terms, the concentration must be higher for higher temperatures.

The LODs at each temperature can be found in Table VI, whereas the LOQs at each temperature can be found in Table VII. These limits are relatively monotonic in temperature as expected as the relatively temperature-insensitive measurement SDs are converted to concentrations using the temperature-compensation calibration equation.

The Turner device has the lowest LOD, in a range of 150%–200% of the specification provided in Table I. The prototype has the highest LOD, though notably, it is also within 150%–200% of the Chelsea TriLux chlorophyll-a LOD of 0.1 ppb, relevant as RWT and chlorophyll-a tend to have similar LODs. This discrepancy can also be attributed to the use of seawater-RWT solutions instead of the usual Milli-Q preparations. The interference from other ions and the degradation of the dye in seawater [7] causes a lower apparent concentration in the standards, which increases the LOD and LOQ.

D. Large Tank Study

The prototype fluorometer was mounted to a BlueROV2 as shown in Fig. 11, along with the AML fluorometer. Both fluorometers are aimed beneath the ROVs ventral side [19].

The sensor integrated ROV was deployed in Dalhousie's Aquatron Laboratory, a 285-m^3 tank of seawater. While the ROV was in the tank, approximately 7 mL of 20% RWT dye (Turner Designs, San Jose, CA, USA) was injected into the tank. The ROV was then arbitrarily driven through the plume and time-series data from the fluorometers were collected. The ROV was then removed from the tank and the tank was cycled
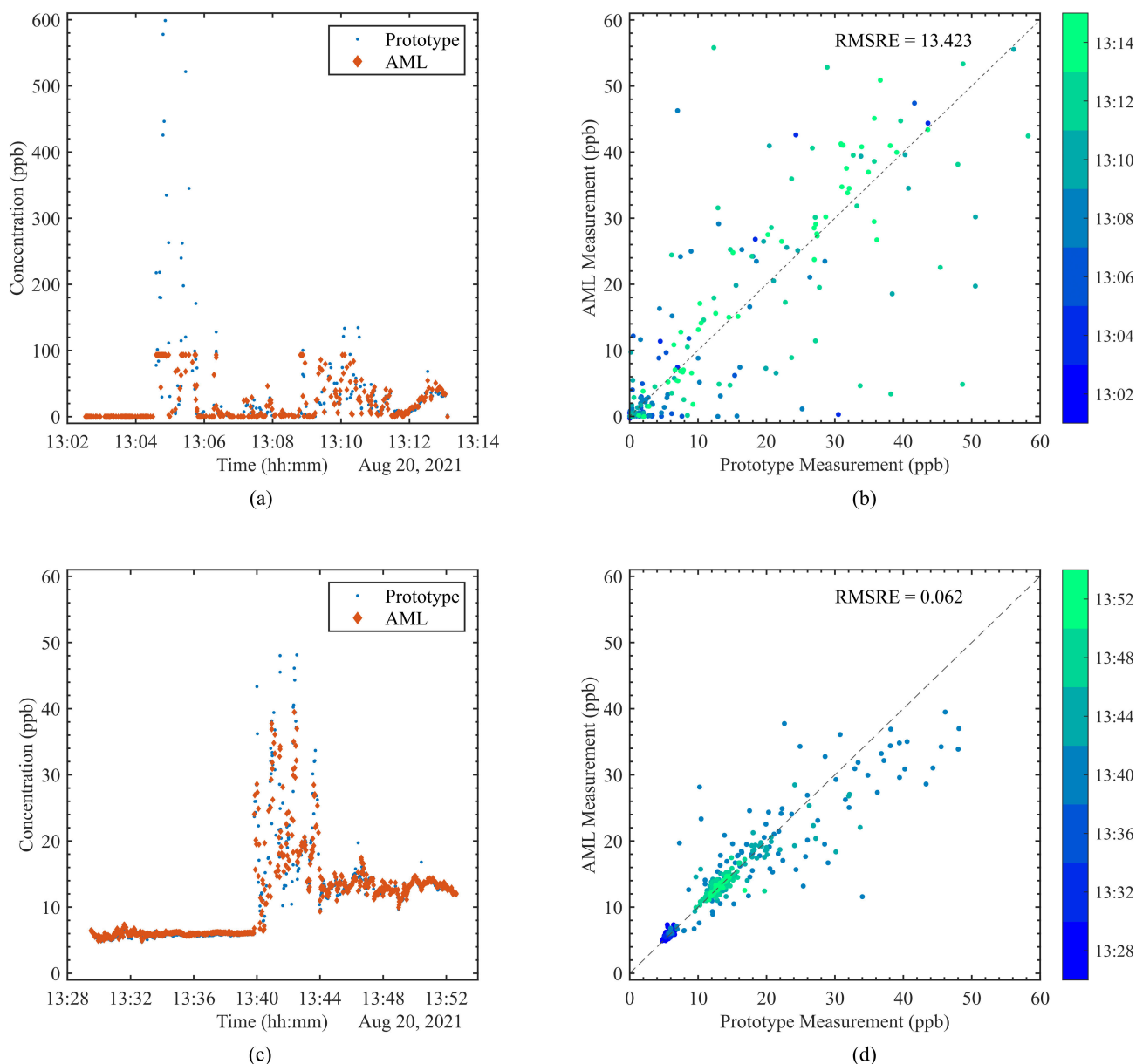
Fig. 12. (a) Plot of the time-series data logged before and during the first dosing of the Aquatron with 7 mL of 20% RWT solution. The increased scattering of data (beginning just after 13:04) indicates the release of the RWT dose. (b) Unity curve comparing the two sensors' data from (a), the prototype on the horizontal and the AML device on the vertical. A color map is included to aid time visualization. The clustering of points shows good agreement prior to the first dose (0 ppb) and divergence as the ROV is piloted through the plume, indicated with a root-mean-squared relative error (RMSRE) of 13.42. (c) Plot of the time-series data logged before and during the second dosing with 7 mL of 20% RWT at 13:40. (d) Unity curve for the data from (c). The clustering of points at 6 ppb shows that the sensors return to good agreement after the tank is cycled to achieve a homogenous RWT concentration. At 13:40, the second dose is added, and the sensor readings diverge, but over time (12 min), both sensors settle toward agreement at 12 ppb, with RMSRE dropping to 0.062.

such that the RWT concentration was uniform throughout. The ROV was then reintroduced to the tank and a second dose of 7 mL of 20% RWT was introduced. As before, the ROV was driven through the plume and the time-series data from the fluorometers were collected.

The time-series results of this test are presented in Fig. 12 along with unity curves illustrating the level of agreement between the two sensors. The first dose time series and the unity curve are presented in Fig. 12(a) and (b), respectively, while the second dose time series and the unity curve are presented in Fig. 12(c) and (d), respectively.

A trend is readily observable from the time series; as the ROV is driving through the plume, the sensor readings diverge significantly, whereas in the homogenous solution (i.e., 0 ppb before the first dose, 6 ppb after the first dose is cycled, and 12 ppb after the second dose has had time to disperse), the sensors agree.

This trend is not an unexpected result: the sensors are spaced approximately 11.5 cm apart and each sensor has a sample volume on the order 1 cm³. Since the viscous RWT plume can have high concentration gradients and the sensors' sample volumes do not overlap, the concentrations recorded by
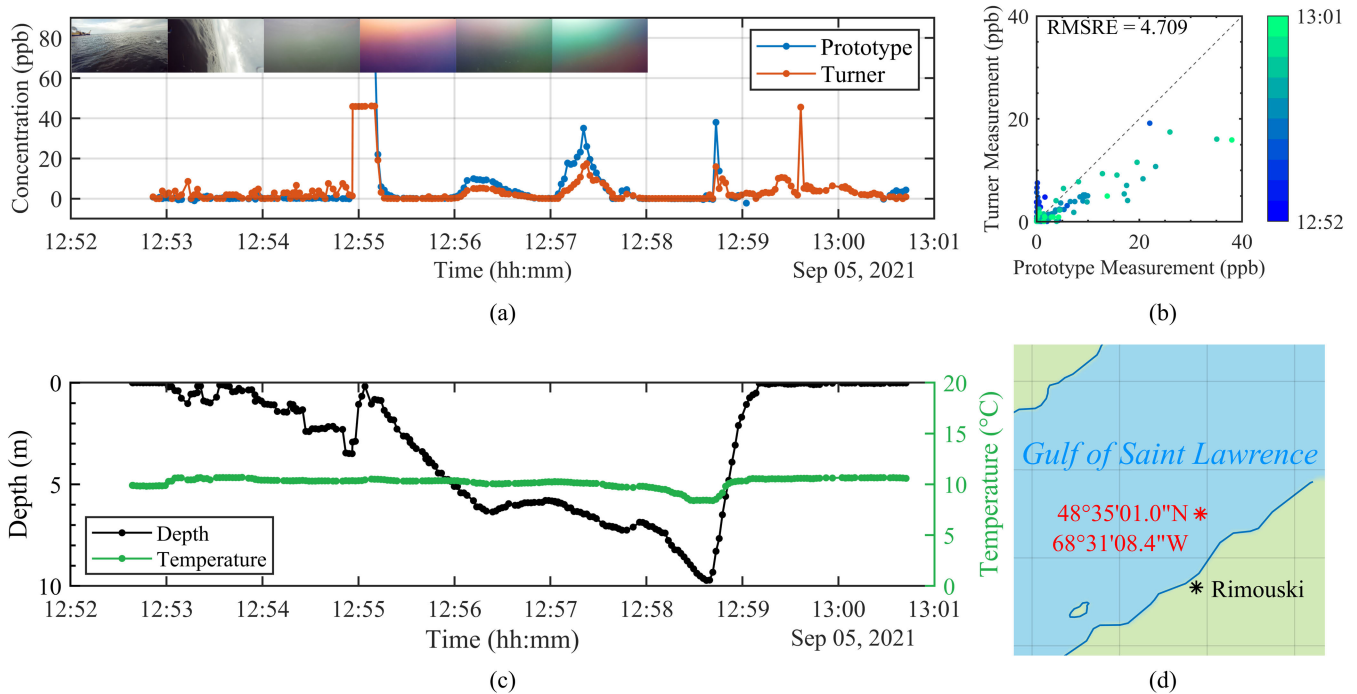
Fig. 13. (a) Plot of RWT fluorometry time series from the TReX deployment; the blue series is the prototype's concentration and the orange series is the Turner device's concentration. Six images are inset, offering time-lapse footage from the ROV front camera, taken from the start of each indicated time point. Data before 12:53 are saturated as the ROV is not submerged prior to this time. (b) Unity curve of the concentration data presented in (a). (c) Plots of depth and ambient temperature recorded by the ROV. (d) Map excerpt indicating the starting coordinates of the ROV upon submersion at 12:53.

each sensor can diverge accordingly, although this divergence diminishes over time as the RWT plume disperses and homogenizes throughout the tank. This is supported by the sharply changing individual readings of each sensor beginning at 13:40 in Fig. 12(c) when the second RWT dose was added. Prior to this time point (i.e., 13:36 to 13:40), the first RWT dose had been cycled in the tank and settled to a uniform concentration of 6 ppb. This is represented by the well-correlated cluster of points at 6 ppb in Fig. 12(d).

By the 13:45 time point, the second RWT dose had settled to an approximately uniform concentration of 12 ppb and the two sensors return to excellent agreement, represented by the well-correlated cluster of points at 12 ppb in Fig. 12(d). This second clustering at 12 ppb is to be expected from the result of cycling the tanks between doses. Each dose contained the same titrated volume of 20% RWT, so the total amount of RWT in the tank after the second dose is twice the amount following the first.

E. Field Deployment

The prototype and Turner fluorometers were mounted to the same BlueROV2 as in the Large Tank study and field-deployed in a dye-tracing measurement application during MEOPAR's 2021 TReX [19].

The TReX is an RWT field experiment focused on time of travel and dispersion data collection for modeling and forecasting. The TReX project is cofunded by the MEOPAR and RQM organizations and is a multidisciplinary effort that integrates inputs from government, academia, and local communities.

In addition to the broad scope of dye-tracer experiments and their applications [8], the MEOPAR website for the TReX project [31] lists ten research works in which the TReX data have been used, with applications, including eddy simulation of surface layer mixing, Langmuir circulation surface drift and dispersion, radar-data estimation of dye dispersion, deep-learning contaminant dispersion, and assessment of oceanic drift prediction models.

Fig. 13 presents the data acquired on the 5th. Fig. 13(a) shows a plot of two time series: the prototype sensor's fluorometry and the Turner analog sensor's fluorometry. Inset onto the plot are time-lapse images from the ROVs' front-facing camera (top left to top center). The images are captured at the start of each minute. For a sanity check, the images were compared to the time-series data; when the fluorometer data peaked, the camera recorded the vivid orange plumes of the RWT dye. When the fluorometer data flattened, the camera recorded images of green-blue seawater. Fig. 13(b) shows a unity curve of the data presented in Fig. 13(a). Fig. 13(c) presents the time series of depth and ambient temperature recorded by the ROV. Fig. 13(d) shows a map image indicating the ROVs' starting coordinates.

Ultimately, the results of the TReX deployment validate the performance of the prototype as a submersible fluorometer and the prototype achieves good agreement with the Turner Cyclops-7 fluorometer.

IV. CONCLUSION

This work presents a prototype low-cost submersible fluorometer that applies a digital lock-in signal processing scheme
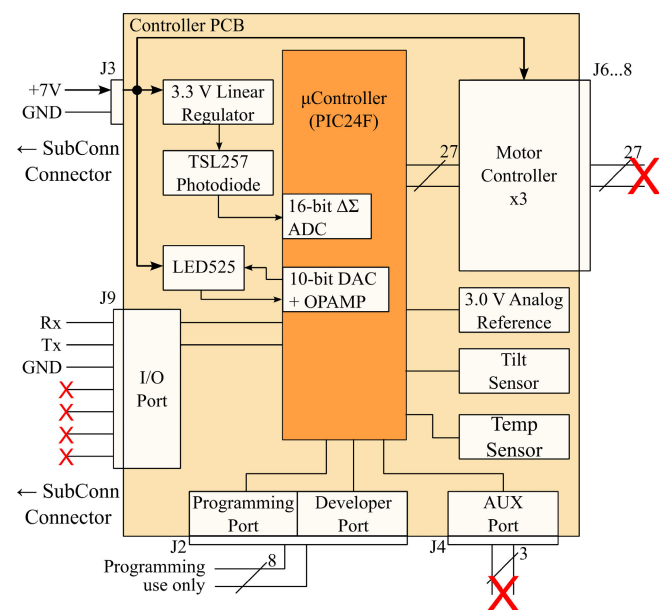
Fig. 14. System architecture block diagram of the custom PCB that controls the prototype fluorometer. The motor controllers and tilt sensor were not required for this fluorometer and added cost without benefit, as this was a legacy and proprietary PCB.

to obtain the performance that is competitive with commercial devices such as the Turner Cyclops-7F fluorometer at a fraction of the cost. The device, when configured for Rhodamine fluorescence, can be assembled for U.S. $744.70 (2022), and with appropriate changes to the custom PCB controller, the price can be further reduced and the performance can be further increased. The LOD of the prototype is below 0.2 ppb, which is comparable to commercially available competitors.

The prototype was successfully mounted to a BlueRobotics BlueROV2 along with its representative competitors for a comparative study in the Dalhousie Aquatron Laboratory and an application to the MEOPAR TReX dye-tracer experiment.

While the initial design of our novel fluorometer targets Rhodamine fluorescence, swapping optoelectronics and optical filters with drop-in alternatives would allow it to target other fluorophores with no added complexity. The demonstrated low-cost fluorometer will facilitate improving our spatiotemporal observation capacity of aquatic environments.

APPENDIX

The system architecture block diagram of the custom PCB that has been repurposed to control the prototype fluorometer is presented in Fig. 14. The controller is printed on a six-layer round circuit board with dimensions matched to the inner diameter of the fluorometer's cast acrylic tube housing.

The controller is based on the PIC24F microcontroller. The integrated 16-bit delta-sigma ADC is used to sample the output of the TSL257 photodiode, whereas the integrated 10-bit DAC and OPAMP form a feedback loop to drive the LED525-33 optical source with the lock-in reference sinusoid.

Power to the device is supplied externally through the six-pin SubConn connector. Of the remaining four pins, three are dedicated to RS-232 data I/O and the last is unused. The LED and photodiode are not placed on the PCB itself; they are interfaced using hook-up wires and are mounted to the 3-D-printed optical stack housings, as shown in Fig. 3(a).

The custom PCB is repurposed from a submersible phosphate analyzer [31] and contains several unused components. The unused sensors, connectors, additional LEDs and photodiodes, and motor driver circuits add cost and layout complexity with no benefit. A functionally identical controller PCB can be realized by simply omitting these components from its design.

REFERENCES

[1] M. Shigemitsu, H. Uchida, T. Yokokawa, K. Arulananthan, and A. Murata, "Determining the distribution of fluorescent organic matter in the Indian ocean using in situ fluorometry," *Frontiers Microbiol.*, vol. 11, Dec. 2020, Art. no. 589262, doi: 10.3389/fmicb.2020.589262.

[2] S. Pärt, H. Kankaanpää, J.-V. Björkqvist, and R. Uiboupin, "Oil spill detection using fluorometric sensors: Laboratory validation and implementation to a FerryBox and a moored SmartBuoy," *Frontiers Mar. Sci.*, vol. 8, p. 1753, Nov. 2021, doi: 10.3389/fmars.2021.778136.

[3] D. M. Anderson, P. Andersen, V. M. Bricelj, J. J. Cullen, and J. E. J. Rensel, *Monitoring and Management Strategies for Harmful Algal Blooms in Coastal Waters*, document #201-MR-01.1, Intergovernmental Oceanographic Commission Technical Series, APEC, Paris, France, 2001.

[4] F. E. Hoge, C. W. Wright, T. M. Kana, R. N. Swift, and J. K. Yungel, "Spatial variability of oceanic phycoerythrin spectral types derived from airborne laser-induced fluorescence emissions," *Appl. Opt.*, vol. 37, no. 21, pp. 4744–4749, Jul. 1998, doi: 10.1364/ao.37.004744.

[5] B. B. Taylor, M. H. Taylor, T. Dinter, and A. Bracher, "Estimation of relative phycoerythrin concentrations from hyperspectral underwater radiance measurements—A statistical approach," *J. Geophys. Res., Oceans*, vol. 118, no. 6, pp. 2948–2960, Jun. 2013, doi: 10.1002/jgrc.20201.

[6] T. R. Miller, W. Tarpey, J. Nuese, and M. Smith, "Real-time monitoring of cyanobacterial harmful algal blooms with the panther buoy," *ACS ES&T Water*, vol. 2, no. 6, pp. 1099–1110, May 2022, doi: 10.1021/acsestwater.2c00072.

[7] P. L. Smart and I. M. S. Laidlaw, "An evaluation of some fluorescent dyes for water tracing," *Water Resour. Res.*, vol. 13, no. 1, pp. 15–33, Feb. 1977, doi: 10.1029/WR013i001p00015.

[8] J. F. Wilson, E. D. Cobb, and F. A. Kilpatrick, "Fluorometric procedures for dye tracing," in *U.S. Geological Survey Techniques of Water Resources Investigations*. Valley Drive Reston, VA, USA: U.S. Geological Survey, 1986, ch. 12, p. 34.

[9] J. E. G. Wheaton, D. Griffiths, and R. C. M. Learner, "Underwater fluorometer measuring system," U.S. Patent 4 293 225, Jun. 29, 1979.

[10] M. Kishino, J. Ishizaka, S.-I. Saitoh, Y. Senga, and M. Utashima, "Verification plan of ocean color and temperature scanner atmospheric correction and phytoplankton pigment by moored optical buoy system," *J. Geophys. Res., Atmos.*, vol. 102, no. D14, pp. 17197–17207, Jul. 1997, doi: 10.1029/96JD04008.

[11] G. P. Klinkhammer, C. S. Chin, C. Wilson, M. D. Rudnicki, and C. R. German, "Distributions of dissolved manganese and fluorescent dissolved organic matter in the Columbia River estuary and plume as determined by in situ measurement," *Mar. Chem.*, vol. 56, nos. 1–2, pp. 1–14, Feb. 1997, doi: 10.1016/S0304-4203(96)00079-5.

[12] P. J. Ralph, R. Gademann, and W. C. Dennison, "In situ seagrass photosynthesis measured using a submersible, pulse-amplitude modulated fluorometer," *Mar. Biol.*, vol. 132, no. 3, pp. 367–373, Oct. 1998, doi: 10.1007/s002270050403.

[13] E. L. Kuniansky, J. M. Blackstock, D. M. Wagner, and J. Van Brahana, "Interpretation of dye tracing data collected November 13-December 2, 2017, at the savoy experimental watershed as part of the advanced groundwater field techniques in Karst Terrains Course, Savoy, Arkansa," U.S. Geological Survey, Reston, VA, USA, Tech. Rep. 2019-5016, 2019.

[14] J. L. Hixson and A. S. Ward, "Hardware selection and performance of low-cost fluorometers,," *Sensors*, vol. 22, no. 6, pp. 2319–2331, Mar. 2022, doi: 10.3390/s22062319.

[15] M. D. Pires, "Evaluation of fluorometers for the in situ monitoring of chlorophyll and/or cyanobacteria," Deltares, Delft, The Netherlands, Tech. Rep. 1203593-000, 2010.

[16] J. A. Busch, J. Engel, O. Zielinski, and A. Friedrichs. (2013). *Review of State of the Art in Affordable Fluorescence Sensors*. CIT-CLOPS. [Online]. Available: http://www.citclops.eu/the-project/public-deliverables

[17] S. E. Zieger, G. Mistlberger, L. Troi, A. Lang, F. Confalonieri, and I. Klimant, "Compact and low-cost fluorescence based flow-through analyzer for early-stage classification of potentially toxic algae and in situ semiquantification," *Environ. Sci. Technol.*, vol. 52, no. 13, pp. 7399–7408, Jun. 2018, doi: 10.1021/acs.est.8b00578.

[18] M. A. Haidekker, K. Dong, E. Mattos, and M. W. van Iersel, "A very low-cost pulse-amplitude modulated chlorophyll fluorometer," *Comput. Electron. Agricult.*, vol. 203, Dec. 2022, Art. no. 107438, doi: 10.1016/j.compag.2022.107438.

[19] J. J. Creelman, "Low-cost submersible fluorometer for fresh and marine water environments," M.S. thesis, Elect. Comput. Eng. Dept., Dalhousie Univ., Halifax, NS, Canada, 2022. [Online]. Available: https://dalspace.library.dal.ca/bitstream/handle/10222/82164/JoshuaCreelman2022.pdf?sequence=3

[20] D. Magde, G. E. Rojas, and P. G. Seybold, "Solvent dependence of the fluorescence lifetimes of xanthene dyes," *Photochem. Photobiol.*, vol. 70, no. 5, pp. 737–744, Nov. 1999, doi: 10.1111/j.1751-1097.1999.tb08277.x.

[21] L. B. McGOWN and K. Nithipatikom, "Molecular fluorescence and phosphorescence," *Appl. Spectrosc. Rev.*, vol. 35, no. 4, pp. 353–393, Nov. 2000, doi: 10.1081/ASR-100101229.

[22] M. Savarese et al., "Fluorescence lifetimes and quantum yields of rhodamine derivatives: New insights from theory and experiment," *J. Phys. Chem. A*, vol. 116, no. 28, pp. 7491–7497, Jul. 2012, doi: 10.1021/jp3021485.

[23] E. C. Minor, E. James, J. A. Austin, V. Nelson, R. Lusk, and K. Mopper, "A preliminary examination of an in situ dual dye approach to measuring light fluxes in lotic systems," *Limnology Oceanography, Methods*, vol. 11, no. 12, pp. 631–642, Dec. 2013, doi: 10.4319/lom.2013.11.631.

[24] G. D. P. Stanchieri, A. De Marcellis, G. Battisti, M. Faccio, E. Palange, and U. Guler, "A 1.8 V low-power low-noise high tunable gain TIA for CMOS integrated optoelectronic biomedical applications," *Electronics*, vol. 11, no. 8, pp. 1271–1281, Apr. 2022, doi: 10.3390/electronics11081271.

[25] V. J. Sieben, C. F. A. Floquet, I. R. G. Ogilvie, M. C. Mowlem, and H. Morgan, "Microfluidic colourimetric chemical analysis system: Application to nitrite detection," *Anal. Methods*, vol. 2, no. 5, pp. 484–491, Feb. 2010, doi: 10.1039/C002672G.

[26] E. A. Luy, S. C. Morgan, J. J. Creelman, B. J. Murphy, and V. J. Sieben, "Inlaid microfluidic optics: Absorbance cells in clear devices applied to nitrite and phosphate detection," *J. Micromech. Microeng.*, vol. 30, no. 9, Jun. 2020, Art. no. 095001, doi: 10.1088/1361-6439/ab9202.

[27] B. J. Murphy, E. A. Luy, K. L. Panzica, G. Johnson, and V. J. Sieben, "An energy efficient thermally regulated optical spectroscopy cell for lab-on-chip devices: Applied to nitrate detection," *Micromachines*, vol. 12, no. 8, pp. 861–875, Jul. 2021, doi: 10.3390/mi12080861.

[28] J. J. Creelman, E. A. Luy, G. C. H. Beland, C. Sonnichsen, and V. J. Sieben, "Simultaneous absorbance and fluorescence measurements using an inlaid microfluidic approach," *Sensors*, vol. 21, no. 18, p. 6250, Sep. 2021, doi: 10.3390/s21186250.

[29] E. J. Arar and G. B. Collins, *Method 445.0 in Vitro Determination of Chlorophyll a and Pheophytin Ain Marine and Freshwater Algae by Fluorescence*. Washington, DC, USA: U.S. Environmental Protection Agency, Sep. 1997.

[30] A. Shrivastava and V. B. Gupta, "Methods for the determination of limit of detection and limit of quantitation of the analytical methods," *Chronicles Young Scientists*, vol. 2, no. 1, pp. 21–25, Apr. 2011, doi: 10.4103/2229-5186.79345.

[31] MEOPAR. *Tracer Release Experiment (TReX)*. MEOPAR. Accessed: Apr. 24, 2023. [Online]. Available: https://meopar.ca/research-trex/

[32] S. Morgan, E. Luy, A. Furlong, and V. Sieben, "A submersible phosphate analyzer for marine environments based on inlaid microfluidics," *Anal. Methods*, vol. 14, no. 1, pp. 22–33, Dec. 2021, doi: 10.1039/D1AY01876K.

Kyle T. Park (Member, IEEE) received the B.Eng. degree in electrical engineering from Dalhousie University, Halifax, NS, Canada, in 2013, where he is currently pursuing the Ph.D degree in electrical engineering.

His research interests include optics and photonics, sensing and instrumentation, embedded system hardware and software design, and digital signal analysis.

Mr. Park was a Charter Member of the IEEE Eta Kappa Nu (HKN) Student Honors Society, Lambda-Theta chapter at Dalhousie.

Joshua J. Creelman received the B.S. and M.A.Sc. degrees in electrical and computer engineering from Dalhousie University, Halifax, NS, Canada, in 2019 and 2023, respectively.

In 2019, he was a Research Assistant with Sieben Laboratories, Halifax. His research interests include sensor technologies, robotics, embedded systems, and biomedical instrumentation.

Allison S. Chua received the B.Eng. degree in mechanical engineering and the M.A.Sc. degree in materials engineering from Dalhousie University, Halifax, NS, Canada, in 2011 and 2014, respectively, where she is currently pursuing the Ph.D. degree in oceanography under the supervision of Dr. Douglas Wallace, Canada Excellence Research Chair (CERC) in Ocean Science and Technology.

Her master's research was in the field of powder metallurgy (PM) under a Boeing Research and Technology grant to develop novel aluminum PM alloys for application in the aerospace industry. After obtaining her M.A.Sc. degree, she worked as a Production Engineer with Irving Shipbuilding Inc., Halifax, where she was responsible for the implementation of piping and mechanical systems for Canada's Arctic Offshore Patrol Ships (AOPS). Her research focuses on the development and application of remote and autonomous underwater platforms for the spatial and temporal characterization of ocean phenomena. For further information, please visit "www.adozenautomobilesandkites.com."

Teala S. Chambers received the B.Sc. degree in ocean sciences from Dalhousie University, Halifax, NS, Canada, in 2021, where she is currently pursuing the M.Sc. degree in oceanography under the supervision of Dr. Douglas Wallace, Canada Excellence Research Chair (CERC) in Ocean Science and Technology.

Her honors research focused on the use of remotely operated underwater vehicles (ROVs) for coastal pond characterization, incorporating quantitative measurements and social science to explore the usefulness of an ROV for coastal community ocean observations. Her research focuses on using novel technology to explore the distribution of redox-sensitive elements in a coastal anoxic basin.

Aaron M. MacNeill (Member, IEEE) received the B.Eng. degree from Dalhousie University, Halifax, NS, Canada, in 2010, and the M.A.Sc. and Ph.D. degrees from Dalhousie University, in 2012 and 2017 respectively, all in electrical engineering.

He is presently an Adjunct Professor with the Electrical and Computer Engineering Department and an Electrical Engineer with the Oceanography Department, Dalhousie University. His research interests include ocean technology, offshore renewable energy, embedded system hardware and software design, and control systems.

Vincent J. Sieben received the Ph.D. degree from the University of Alberta, Edmonton, AB, Canada, in 2008.

From 2008 to 2011, Dr. Sieben conducted pioneering research on microfluidic bio/chemical sensors with the National Oceanography Center, Southampton, U.K. Subsequently, he spent seven years in industry as a Scientist commercializing microfluidics for Schlumberger, Cambridge, MA. USA. Dr. Sieben currently leads the Ocean Sensors Laboratory, Dalhousie University, Halifax, NS, Canada, where he is also an Associate Professor with the Electrical and Computer Engineering Department.